Scaling laws of the plasma velocity in visco-resistive magnetohydrodynamic systems

A Krupka, M.-C Firpo

Scaling laws of the plasma velocity in visco-resistive magnetohydrodynamic systems

A. Krupka, M.-C. Firpo*

Laboratoire de Physique des Plasmas (LPP), CNRS, Sorbonne Université, École polytechnique, Institut Polytechnique de Paris, 91120 Palaiseau, France

Abstract

We consider a visco-resistive magnetohydrodynamic modeling of a steady-state incompressible tokamak plasma with a prescribed toroidal current drive, featuring constant resistivity η and viscosity ν. It is shown that the plasma velocity root-mean-square behaves as $\eta f(H)$ as long as the inertial term remains negligible, where H stands for the Hartmann number $H \equiv (\eta\nu)^{-1/2}$, and that $f(H)$ exhibits power-law behaviours in the limits $H \ll 1$ and $H \gg 1$. In the latter limit, we establish that $f(H)$ scales as $H^{1/4}$, which is consistent with numerical results.

Keywords: magnetic confinement fusion, plasma rotation, scaling laws

1. Introduction

The rotation of plasma has been identified as a possible key factor in the heat and particle confinement properties of tokamaks. High-velocity rotation could propose a way to avoid, stabilize, or quench instabilities in the system. It has, for instance, been predicted to stabilize external modes when the plasma rotates at some fraction of the sound speed [1], yet significantly lower stabilization thresholds have been obtained in some experimental conditions [2, 3]. Moreover, numerous experimental observations have supported the existence of some intrinsic plasma rotation in connection with the high-confinement mode [4], essentially related to the existence of an $\mathbf{E} \times \mathbf{B}$ velocity with a radial electric field, although further investigation would be needed to assert whether plasma rotation does play the role of an actuator in this specific phenomenon. Intrinsic rotation has also been observed in the L-mode [5]. Understanding and controlling the plasma rotation are, in any case, important research objectives towards achieving enhanced plasma performance and sustainable fusion reactions in tokamak devices. To address this matter, we reconsider here the derivation of the axisymmetric steady-states of the visco-resistive magnetohydrodynamic (MHD) equations without making a no-flow hypothesis. This means that we reintroduce in the traditional Grad-Shafranov equation the dissipative viscous term and the nonlinear $(\mathbf{v} \cdot \nabla)\mathbf{v}$ term coming from the steady-state Navier-Stokes equation [6, 7, 8, 9, 10, 11, 12]. In Section 2, we propose a step-by-step derivation of the dimensionless closed system of partial differential equations, first introduced in [6] to model tokamak plasmas within a magnetohydrodynamic visco-resistive setting. Let us emphasize here that this model obviously bears the limitations inherent to any magnetohydrodynamic (MHD), and thus non-kinetic, approach. Following the derivation of this system, coupling the steady-state Maxwell equations to the steady-state Navier-Stokes equation with Ohm's law closure, we focus on the behavior of the system for a constant toroidal current drive in Section 2.4 and derive a scaling law for the velocity that is expected to be valid as long as the magnitude of the inertial $\boldsymbol{\omega} \times \mathbf{v}$ term is small enough. This prediction is tested on numerical simulations in Sections 3 and 4. These use the finite element method through the open-source platform FreeFem++ for solving partial differential equations [13]. A conclusive Section 5 summarizes the outcomes of the study.

2. Axisymmetric steady-states in the visco-resistive incompressible MHD setting under tokamak-like drives

2.1. Derivation of the dimensionless system of partial differential equations

Let us first propose a step-by-step derivation of the single fluid magnetohydrodynamic (MHD) description of steady-state tokamak plasmas without proceeding to a zero velocity assumption. Denoting by ρ_m, the total mass density of plasma, by n_i the number density of ions, by n_e the number density of electrons, by ρ the electric charge density, by p the plasma pressure, by $\mathbf{v}$ the flow velocity of plasma and by $\mathbf{j}$ the current density, one obtains the following identities

$$\begin{aligned}
\rho_m &= n_i m_i \left(1 + \frac{m_e}{m_i} Z\right), \\
\rho &= -e\,(n_e - Z n_i)\,, \\
p &= p_i + p_e, \\
\mathbf{v} &= \mathbf{v}_i + \frac{m_e}{m_i} Z\,(\mathbf{v}_e - \mathbf{v}_i)\,, \\
\mathbf{j} &= -e n_e\,(\mathbf{v}_e - \mathbf{v}_i)\,.
\end{aligned}$$

The steady-state equation of motion ($\partial/\partial t = 0$) for the one-fluid model is

$$\rho_m\,(\mathbf{v} \cdot \nabla)\,\mathbf{v} = -\nabla p + \rho\mathbf{E} + \mathbf{j} \times \mathbf{B} + \mu\nabla^2\mathbf{v}. \tag{1}$$

*Corresponding author

Email addresses: anna.krupka@lpp.polytechnique.fr (A. Krupka), marie-christine.firpo@lpp.polytechnique.fr (M.-C. Firpo)

with

$$(\mathbf{v}\cdot\nabla)\,\mathbf{v} = \nabla\left(\frac{v^2}{2}\right) + \boldsymbol{\omega}\times\mathbf{v} \tag{2}$$

where $\boldsymbol{\omega}$ is the vorticity vector that $\boldsymbol{\omega} = \nabla\times\mathbf{v}$.
Assuming electroneutrality ($\rho = 0$), this gives

$$\rho_m\boldsymbol{\omega}\times\mathbf{v} = -\nabla p^* + \mathbf{j}\times\mathbf{B} + \mu\nabla^2\mathbf{v} \tag{3}$$

with

$$p^* = p + \rho_m\frac{v^2}{2}. \tag{4}$$

Introducing the kinematic viscosity $\nu = \mu/\rho_m$, this amounts to

$$\boldsymbol{\omega}\times\mathbf{v} = -\nabla\left(\frac{p^*}{\rho_m}\right) + \rho_m^{-1}\mathbf{j}\times\mathbf{B} + \nu\nabla^2\mathbf{v} \tag{5}$$

with

$$\nabla\times\mathbf{B} = \mu_0\mathbf{j}. \tag{6}$$

Ohm's law reads

$$\mathbf{E} + \mathbf{v}\times\mathbf{B} = \eta\mathbf{j}. \tag{7}$$

Let us now assume that the plasma is incompressible, which means its mass density is constant $\rho = \rho_{m0}$. Let us introduce the dimensionless variables $\hat{\mathbf{v}} = \mathbf{v}/v_{A0} = \mathbf{v}/b_0$ and $\hat{\mathbf{b}} = \mathbf{b}/b_0$, where $\mathbf{b} = \mathbf{v}_A = \mathbf{B}/\sqrt{\mu_0\rho_{m0}}$ with the Alfvén velocity $v_{A0} = b_0$ defined by

$$b_0 = \frac{B_0}{\sqrt{\mu_0\rho_{m0}}} \tag{8}$$

and $\hat{\nabla} = r_0\nabla$, where r_0 denotes the tokamak major radius. Let us then also define the spatial variables rescaled by r_0, so that the horizontal and vertical coordinates are $x = r/r_0$ and $y = z/r_0$. As we are focusing on axisymmetric toroidal-invariant steady-states, all spatial dependence can be expressed in the variables x and y and the integration domain will be the tokamak plasma poloidal cross-section (see Sect. 3.1). This gives

$$\left(\hat{\nabla}\times\hat{\mathbf{v}}\right)\times\hat{\mathbf{v}} = -\hat{\nabla}\left(\hat{p^*}\right) + \left(\hat{\nabla}\times\hat{\mathbf{b}}\right)\times\hat{\mathbf{b}} + \hat{\nu}\hat{\nabla}^2\hat{\mathbf{v}} \tag{9}$$

with the dimensionless viscosity

$$\hat{\nu} = \frac{\nu}{b_0 r_0}, \tag{10}$$

and dimensionless total pressure

$$\hat{p^*} = \frac{p^*}{b_0^2\rho_m}. \tag{11}$$

As for the Ohm's law, we have

$$\frac{E_0}{x}\mathbf{i}_\varphi - \nabla\Phi + b_0^2\sqrt{\mu_0\rho_{m0}}\hat{\mathbf{v}}\times\hat{\mathbf{b}} = \frac{\eta\sqrt{\mu_0\rho_{m0}}}{\mu_0}b_0 r_0\hat{\nabla}\times\hat{\mathbf{b}} \tag{12}$$

with $\mathbf{E} = \frac{E_0}{x}\mathbf{i}_\varphi - \nabla\Phi$ (so that $\nabla\times\mathbf{E} = 0$). Taking the curl of the Ohm's law, we get

$$b_0^2\sqrt{\mu_0\rho_{m0}}\hat{\nabla}\times\left(\hat{\mathbf{v}}\times\hat{\mathbf{b}}\right) = \frac{\eta\sqrt{\mu_0\rho_{m0}}}{\mu_0}b_0 r_0^{-1}\hat{\nabla}\times\left(\hat{\nabla}\times\hat{\mathbf{b}}\right). \tag{13}$$

Consequently, the rescaled resistivity $\hat{\eta}$ should be such that

$$\hat{\eta} = \frac{\eta}{\mu_0 r_0 b_0}. \tag{14}$$

The full Ohm's law reads then

$$\left(b_0^2\sqrt{\mu_0\rho_{m0}}\right)^{-1}\left(\frac{E_0}{x}\mathbf{i}_\varphi - \nabla\Phi\right) + \hat{\mathbf{v}}\times\hat{\mathbf{b}} = \hat{\eta}\hat{\nabla}\times\hat{\mathbf{b}} \tag{15}$$

so that the rescaled, dimensionless, electric field is such that

$$\hat{E}_0 = \frac{E_0}{b_0^2\sqrt{\mu_0\rho_{m0}}} \tag{16}$$

with

$$\frac{\hat{E}_0}{x}\mathbf{i}_\varphi - \hat{\nabla}\hat{\Phi} + \hat{\mathbf{v}}\times\hat{\mathbf{b}} = \hat{\eta}\hat{\nabla}\times\hat{\mathbf{b}}. \tag{17}$$

Summarizing, we have with $\hat{\omega} = \hat{\nabla}\times\hat{\mathbf{v}}$ and $\hat{\mathbf{j}} = \hat{\nabla}\times\hat{\mathbf{b}}$,

$$\hat{\omega}\times\hat{\mathbf{v}} = -\hat{\nabla}\left(\frac{p^*}{b_0^2\rho_m}\right) + \hat{\mathbf{j}}\times\hat{\mathbf{b}} + \hat{\nu}\hat{\nabla}^2\hat{\mathbf{v}} \tag{18}$$

$$\frac{\hat{E}_0}{x}\mathbf{i}_\varphi - \hat{\nabla}\hat{\Phi} + \hat{\mathbf{v}}\times\hat{\mathbf{b}} = \hat{\eta}\hat{\mathbf{j}} \tag{19}$$

with

$$\hat{\nabla}\cdot\hat{\mathbf{v}} = 0,$$
$$\hat{\nabla}\cdot\hat{\mathbf{b}} = 0.$$

Writing

$$\mathbf{B} = \hat{\nabla}\frac{\chi}{r_0}\times\frac{1}{r_0 x}\mathbf{i}_\varphi + \left(B_0\frac{r_0}{r} + B_\varphi\right)\mathbf{i}_\varphi \tag{20}$$

so that

$$\hat{\mathbf{b}} = \frac{1}{x}\hat{\nabla}\hat{\chi}\times\mathbf{i}_\varphi + \left(\frac{1}{x} + \hat{b}_\varphi\right)\mathbf{i}_\varphi, \tag{21}$$

where the rescaled magnetic flux is

$$\hat{\chi} = \frac{\chi}{B_0 r_0^2}, \tag{22}$$

ensures that Gauss's equation is satisfied. Ampère's law gives

$$\hat{\mathbf{j}} = \frac{1}{x}\hat{\nabla}\left(x\hat{b}_\varphi\right)\times\mathbf{i}_\varphi - \frac{1}{x}\left(\hat{\triangle}^*\hat{\chi}\right)\mathbf{i}_\varphi \tag{23}$$

where the operator $\hat{\triangle}^*$ is defined by

$$\hat{\triangle}^* A = \hat{\nabla}^2 A - \frac{2}{x}\frac{\partial A}{\partial x} = \frac{\partial^2 A}{\partial x^2} - \frac{1}{x}\frac{\partial A}{\partial x} + \frac{\partial^2 A}{\partial y^2}. \tag{24}$$

We have

$$\mathbf{v} = \hat{\nabla}\frac{\psi}{r_0}\times\frac{1}{r_0 x}\mathbf{i}_\varphi + v_\varphi\mathbf{i}_\varphi \tag{25}$$

so that

$$\hat{\mathbf{v}} = \frac{1}{x}\hat{\nabla}\hat{\psi}\times\mathbf{i}_\varphi + \hat{v}_\varphi\mathbf{i}_\varphi \tag{26}$$

with

$$\hat{\psi} = \frac{\psi}{b_0 r_0^2}. \tag{27}$$

And the dimensionless vorticity reads

$$\hat{\omega} = \frac{1}{x}\hat{\nabla}\left(x\hat{v}_\varphi\right)\times\mathbf{i}_\varphi - \frac{1}{x}\left(\hat{\triangle}^*\hat{\psi}\right)\mathbf{i}_\varphi. \tag{28}$$

The toroidal part of Eq. (28) gives

$$\hat{\triangle}^*\hat{\psi} = -x\hat{\omega}_\varphi. \tag{29}$$

Taking the curl of the force balance one obtains

$$\hat{\nabla}\times\left(\hat{\omega}\times\hat{\mathbf{v}} - \hat{\mathbf{j}}\times\hat{\mathbf{b}}\right) = \hat{\nu}\hat{\nabla}^2\hat{\omega}. \tag{30}$$

Defining $\tilde{u}_1 = \hat{\psi}$, $u_2 = x\hat{\omega}_\varphi$, $\tilde{u}_3 = x\hat{b}_\varphi + 1$, $\tilde{u}_4 = x\hat{v}_\varphi$, $\tilde{u}_5 = \hat{\chi}$, $\tilde{u}_6 = x\hat{j}_\varphi$, Eq. (29) reads

$$\hat{\triangle}^*\tilde{u}_1 = -u_2. \tag{31}$$

Here we would like to introduce the Poisson bracket $\{u, v\}$ for any space functions u and v by

$$\{u, v\} = \frac{\partial u}{\partial x}\frac{\partial v}{\partial y} - \frac{\partial v}{\partial x}\frac{\partial u}{\partial y}. \tag{32}$$

We get from the toroidal part of the curl of the force balance (30)

$$\hat{\nu}\hat{\triangle}^*u_2 = \frac{1}{x^2}\frac{\partial}{\partial y}(\tilde{u}_3^2 - \tilde{u}_4^2) + \frac{1}{x}\{\tilde{u}_6, \tilde{u}_5\} + \frac{1}{x}\{\tilde{u}_1, u_2\} + \frac{2u_2}{x^2}\frac{\partial\tilde{u}_1}{\partial y} - \frac{2\tilde{u}_6}{x^2}\frac{\partial\tilde{u}_5}{\partial y}. \tag{33}$$

The curl of Ohm's law gives

$$\hat{\nabla}\times\left(\hat{\mathbf{v}}\times\hat{\mathbf{b}}\right) = \hat{\eta}\hat{\nabla}\times\hat{\mathbf{j}} \tag{34}$$

which yields along the toroidal direction

$$\hat{\eta}\hat{\triangle}^*u_3 = \frac{1}{x}\{\tilde{u}_1, \tilde{u}_3\} + \frac{1}{x}\{\tilde{u}_4, \tilde{u}_5\} + \frac{2\tilde{u}_3}{x^2}\frac{\partial\tilde{u}_1}{\partial y} - \frac{2\tilde{u}_4}{x^2}\frac{\partial\tilde{u}_5}{\partial y}. \tag{35}$$

The toroidal part of the force balance equation (18) under the axisymmetric hypothesis yields

$$\left(\hat{\nu}\hat{\nabla}^2\hat{\mathbf{v}}\right)\cdot\mathbf{i}_\varphi = \left(\hat{\omega}\times\hat{\mathbf{v}} - \hat{\mathbf{j}}\times\hat{\mathbf{b}}\right)\cdot\mathbf{i}_\varphi \tag{36}$$

giving

$$\hat{\nu}\hat{\triangle}^*\tilde{u}_4 = \frac{1}{x}\{\tilde{u}_1, \tilde{u}_4\} + \frac{1}{x}\{\tilde{u}_3, \tilde{u}_5\}. \tag{37}$$

And finally, we have the counterpart of Eq. (31) for the magnetics, namely

$$\hat{\triangle}^*\tilde{u}_5 = -\tilde{u}_6. \tag{38}$$

The toroidal part of Ohm's law finally gives

$$\frac{\hat{E}_0}{x} + \left(\hat{\mathbf{v}}\times\hat{\mathbf{b}}\right)\cdot\mathbf{i}_\varphi = \hat{\eta}\hat{\mathbf{j}}\cdot\mathbf{i}_\varphi \tag{39}$$

that is

$$\hat{\eta}\tilde{u}_6 = \hat{E}_0 + \frac{1}{x}\{\tilde{u}_5, \tilde{u}_1\}. \tag{40}$$

2.2. Toroidal current drive

In order to be consistent with the notations of [6], let us introduce two current characteristic scales, namely the order of magnitude of the current that would be needed in a vertical infinite wire to produce the toroidal magnetic field at the center of the plasma column

$$I_b = \frac{r_0 B_0}{\mu_0} \tag{41}$$

and the order of magnitude of the current involved in Joule heating of the plasma under the loop voltage E_0

$$I_e = \frac{r_0^2 E_0}{\eta}. \tag{42}$$

Using the expressions of the dimensionless resistivity, $\hat{\eta}$ (14), and dimensionless toroidal electric field, $\hat{E}_0$ (16), one obtains

$$\frac{\hat{E}_0}{\hat{\eta}} = \frac{I_e}{I_b}. \tag{43}$$

The calculations of Section 2.1 have just shown that it is not necessary to introduce explicitly these two current characteristic scales in the system of equations. Yet, in the present study, we are interested in the behavior of the system for a given ratio of these (43), namely for a given $\hat{E}_0/\hat{\eta}$. This quantity may be viewed as the only explicit drive appearing in the dimensionless system of equations as written in the following Section 2.3. Equation (43) shows that this control parameter amounts to the ratio of the electric current involved for plasma Ohmic heating over that needed for generating the external toroidal magnetic field.

2.3. Final set of equations

Summarizing the above calculations and dropping some tildes to improve readability, one is left with the system of parabolic partial differential equations of [6]

$$\triangle^*u_1 = -u_2, \tag{44}$$

$$\hat{\nu}\triangle^*u_2 = \frac{1}{x^2}\frac{\partial}{\partial y}(u_3^2 - u_4^2) + \frac{1}{x}\{u_6, u_5\} + \frac{1}{x}\{u_1, u_2\} + \frac{2u_2}{x^2}\frac{\partial u_1}{\partial y} - \frac{2u_6}{x^2}\frac{\partial u_5}{\partial y}, \tag{45}$$

$$\hat{\eta}\triangle^*u_3 = \frac{1}{x}\{u_1, u_3\} + \frac{1}{x}\{u_4, u_5\} + \frac{2u_3}{x^2}\frac{\partial u_1}{\partial y} - \frac{2u_4}{x^2}\frac{\partial u_5}{\partial y}, \tag{46}$$

$$\hat{\nu}\triangle^*u_4 = \frac{1}{x}\{u_1, u_4\} + \frac{1}{x}\{u_3, u_5\}, \tag{47}$$

$$\triangle^*u_5 = -u_6, \tag{48}$$

with

$$\hat{\eta}u_6 = \hat{E}_0 + \frac{1}{x}\{u_5, u_1\}, \tag{49}$$

where all the dimensionless variables have been defined in Section 2.1. From now on, only dimensionless variables will be used, and to simplify notation, we will denote them without the hat symbol.

2.4. Behaviour of the steady-state axisymmetric plasma speed under some given tokamak-like drive

In the present study, we consider the axisymmetric steady-states of the (dimensionless) Navier-Stokes equation

$$\boldsymbol{\omega} \times \mathbf{v} = -\nabla p^* + \mathbf{j} \times \mathbf{b} + \nu \nabla^2 \mathbf{v}, \tag{50}$$

self-consistently satisfying the steady-state Maxwell equations with Ohm's law coupling

$$\mathbf{E} + \mathbf{v} \times \mathbf{b} = \eta \mathbf{j}. \tag{51}$$

In magnetic confinement fusion, η and ν are two small parameters. Combining the equations (50) and (51) yields

$$\boldsymbol{\omega} \times \mathbf{v} = -\nabla p^* + \left(\frac{\mathbf{E}}{\eta} + \eta^{-1} \mathbf{v} \times \mathbf{b} \right) \times \mathbf{b} + \nu \nabla^2 \mathbf{v}. \tag{52}$$

Let us put $\mathbf{v} = (\eta/\nu)^{1/2} \widetilde{\mathbf{v}}$ and, consistently, $\boldsymbol{\omega} = (\eta/\nu)^{1/2} \widetilde{\boldsymbol{\omega}}$. By making this change of variable, Eq. (52) becomes

$$\frac{\eta}{\nu} \widetilde{\boldsymbol{\omega}} \times \widetilde{\mathbf{v}} = -\nabla p^* + \left(\frac{\mathbf{E}}{\eta} + (\eta\nu)^{-1/2} \widetilde{\mathbf{v}} \times \mathbf{b} \right) \times \mathbf{b} + (\eta\nu)^{1/2} \nabla^2 \widetilde{\mathbf{v}}. \tag{53}$$

Using the Hartmann number, H, defined as $H = (\eta\nu)^{-1/2}$, this reads

$$\eta^2 H^2 \widetilde{\boldsymbol{\omega}} \times \widetilde{\mathbf{v}} = -\nabla p^* + \left(\frac{\mathbf{E}}{\eta} + H \widetilde{\mathbf{v}} \times \mathbf{b} \right) \times \mathbf{b} + H^{-1} \nabla^2 \widetilde{\mathbf{v}}. \tag{54}$$

The pressure term can be eliminated by taking the curl of the equation. Let us discuss this equation for a given drive $\mathbf{E}/\eta$. *If* we can neglect the left-hand side inertial term in Eq. (54), then we are left with

$$\nabla \times \left[\left(\frac{\mathbf{E}}{\eta} + H \widetilde{\mathbf{v}} \times \mathbf{b} \right) \times \mathbf{b} + H^{-1} \nabla^2 \widetilde{\mathbf{v}} \right] = \mathbf{0} \tag{55}$$

and, at given $\mathbf{E}/\eta$, plasma velocity $\widetilde{\mathbf{v}}$ must be a function of H only, meaning that $\mathbf{v}/\eta = H\widetilde{\mathbf{v}}$ is a function of H only. This prevalence of the Hartmann number was already inferred in the Reverse Field Pinch [14] where visco-resistive MHD simulations showed that the transition from multiple to quasi-single helicity states is controlled by the Hartmann number. Section 3 will be devoted to the numerical exploration of this dependence of $\mathbf{v}/\eta$ on H only and of its validity domain. Using different values of the resistivity η while keeping constant the drive $\mathbf{E}/\eta$, any change of behaviour in the form of the components of $\mathbf{v}/\eta$, if non-numerical, might be considered as a signal of the onset of nonlinear effects.

Before delving into this, let us briefly consider the neutral fluid case to discuss the onset of inertial effects in Eq. (54). If we introduce the Reynolds number, R_e, as the ratio between the order of magnitude of the inertial over the viscous forces, and assume that the characteristic length of the variation of $\mathbf{v}$ is r_0, then we have

$$R_e = \eta H^2 \nu. \tag{56}$$

To fix ideas, let us remind that, in a circular pipe, the usual (neutral) fluid turbulence sets in for $R_e \geq R_{ec} \simeq 3.10^3$. Consequently, if we take the fusion relevant value $\eta = 10^{-8}$, this (qualitative) threshold would be attained for a velocity Mach number as large as $v_c = 0.3$ at $H = 10^6$, or as low as $v_c = 0.3 \times 10^{-4}$ if $H = 10^8$. This could be an incentive to better estimate viscosity, and thus the Hartmann number, in magnetized plasma flows. However, in the case of a tokamak plasma, the initiation of inertial effects is anticipated to be much different as it is governed by its balance with the Laplace force rather than the dissipative force.

3. Numerical Results

3.1. Domain and boundary conditions

To solve the system of equations described in Eqs. (44)-(49), it is essential to establish and define the computational cross-section plasma domain Ω. In this paper, all simulations are carried out within a 2D JET geometry, meaning that the plasma border is defined by the parametric equations

$$\begin{cases} x = 1 + \dfrac{r_1}{r_0} \cos\left(\theta + \arcsin\delta \sin\theta\right) \\ y = k \dfrac{r_1}{r_0} \sin(\theta) \end{cases} \tag{57}$$

Here $\theta \in [0, 2\pi]$, r_0 is the major radius, r_1 is the semi-minor axis of the cross-section, δ is the triangularity parameter, and k is the plasma elongation. For our simulations, we use typical JET parameters: the major radius is $r_0 = 3$ m, the semi-minor axis radius is $r_1 = 1.25$ m, the plasma elongation $k = 1.55$, and finally $\arcsin\delta = 0.5$. The value of the external toroidal magnetic field denoted as B_0, is set at 2.8 Tesla (T), a setting consistent with the conditions in the JET experiment. The toroidal loop voltage is chosen to be equal to 1 V. This is a reasonable assumption since the toroidal electric field is of the order of some V/m in the current devices. The velocities are scaled using Alfvénic units, where the Alfvén velocity, represented as b_0, is estimated to be approximately 5.5×10^6 meters per second (m/s) according to Eq. (8). Similarly, based on Eq. (16), the normalized electric field, denoted by E_0, is approximated to be of the order of 3.5×10^{-9}.

We now introduce the boundary conditions on $\partial\Omega$. The elliptic system (44)-(48) requires five boundary conditions. The four associated with the divergence-free properties of the magnetic field (**b**), current density (**j**), velocity (**v**), and vorticity (ω) vector fields can be determined by ensuring the continuity of their normal components along the plasma boundary. In the numerical simulations, the following boundary conditions have been selected: $u_1 = u_5 = 0$ and $u_3 = 1$. Concerning u_2 and u_4, a toroidal "no-slip" condition is imposed, with $u_2 = u_4 = 0$. Alternatively, three additional boundary conditions, apart from the toroidal no-slip boundary condition, will be chosen. A free-slip condition, also known as shear-stress free, in the toroidal direction, is represented by the condition $\partial_n(u_4/r^2) = 0, u_2 = 0$. A normal component of toroidal velocity equal to 0 is represented by the condition $\partial_n(u_4/x) = 0, u_2 = 0$. Finally, we shall also enforce Neumann boundary conditions on both the toroidal velocity and toroidal vorticity through $\partial_n(u_4/x) = \partial_n(u_2/x) = 0$.

To solve the system of equations (44)-(49) on the cross-section plasma domain Ω together with boundary conditions,

we use the finite element method through the open-source platform FreeFem++ for solving partial differential equations [13].

3.2. *Preliminary results*

The simulations shown in Figs. 1, 2 and 3 admit a toroidal no-slip boundary condition for the toroidal velocity and a constant ratio E_0/η of order 1. Fig. 1 depicts the computed steady-state toroidal velocity fields for two different Hartmann numbers: $H = 10$ and $H = 10^5$ at a given resistivity η. In Figs. 2 and 3, the root mean squares of the toroidal and poloidal velocity fields are computed for different resistivity values. The numerical results can be separated into three distinct "regimes". In this section we are going to focus on discussing the third regime and its validity.

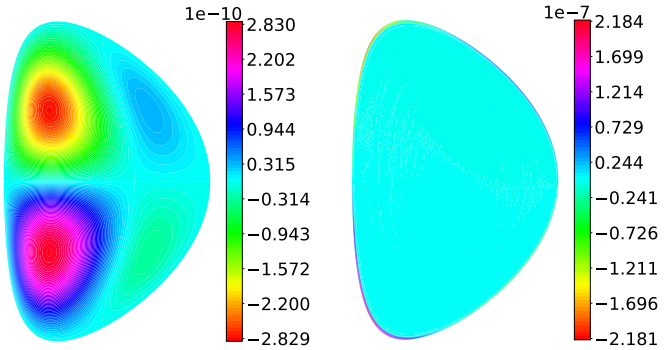

Figure 1: Toroidal velocity field computed with the finite element method (FEM) using FreeFem++ with P1 elements for $H = 10$ (on the left) and $H = 10^5$ (on the right) in JET geometry with no-slip boundary condition for toroidal velocity with η=6.9e-9 and $E_0/\eta = 0.43$.

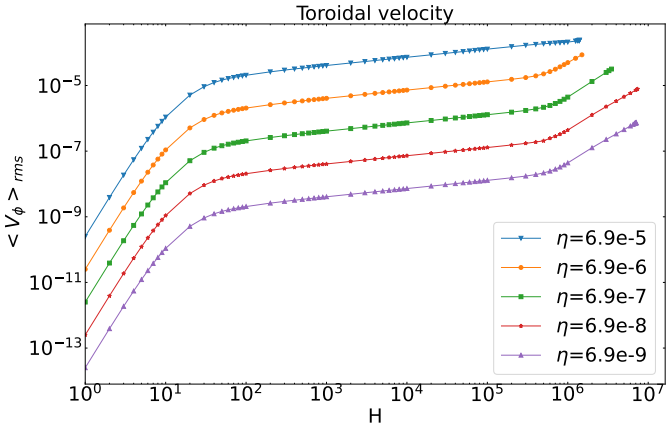

Figure 2: Root-mean square of the toroidal velocity field in Alfvén velocity units as a function of the Hartmann number in log-log scale for different values of the resistivity with no-slip boundary condition for toroidal velocity with $E_0/\eta = 0.43$.

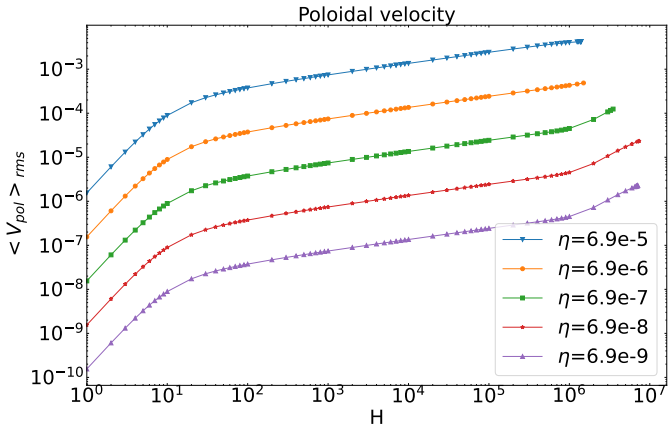

Figure 3: Same as Fig. 2 for the poloidal velocity field.

The log-log plots of Figs. 2 and 3 demonstrate that, at a given E_0/η ratio, the velocity is proportional to the resistivity and to some function depending solely on the Hartmann number. However, the emergence of a third regime at H-values above 10^6 resulting in slight variations of the velocity behaviour for different resistivity values suggests that nonlinear effects may be increasingly significant. In all the figures, the plotted results are, by default, those obtained with the highest resolution (the maximum number of triangles). Fig. 4 illustrates the evolution of numerical results as a function of the number of triangles, N, used. It appears that for values of the Hartmann number beyond 10^6, the results depend on the mesh. This is easily interpreted in light of the large-H cross-section plots of the toroidal velocity field (see Fig. 1).

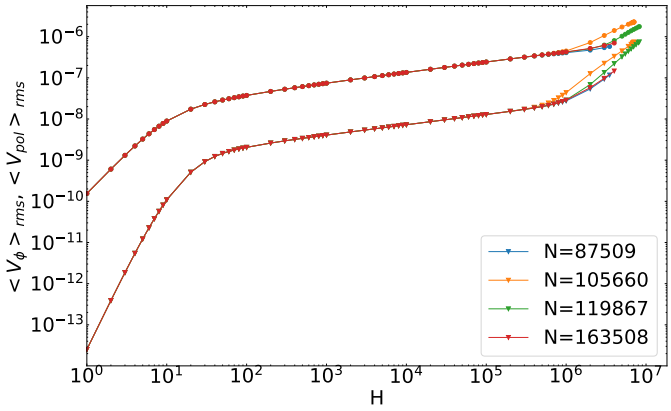

Figure 4: Root-mean square of toroidal and poloidal velocities as a function of the Hartmann number in Alfvén velocity units with η=6.9e-9 for different numbers of triangles with no-slip boundary condition for toroidal velocity.

To obtain robust results, it is necessary to finely resolve the boundary layer appearing at the edge of the domain that characterizes this second regime. With N=163508 triangles, we are approaching the maximum accessible resolution. It is probable, but not certain, based on the simulations in Figure 4, that the end of the scaling law of the second regime is a numerical artifact due to a resolution deficiency.

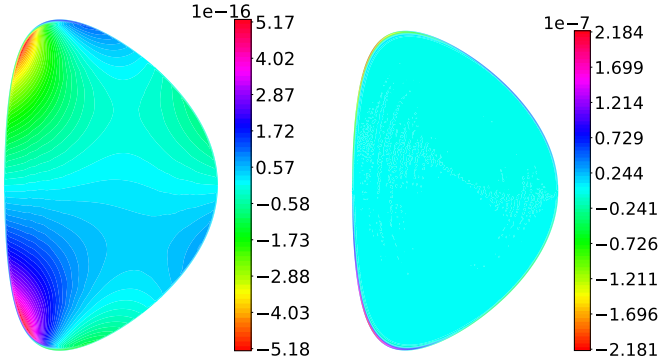

Figure 5: Contribution of $(\boldsymbol{\omega}\times\mathbf{v})\cdot\mathbf{i}_\varphi$ term (on the left) and $(\mathbf{j}\times\mathbf{b})\cdot\mathbf{i}_\varphi$ term (on the right) to the total toroidal velocity for $H = 10^5$.

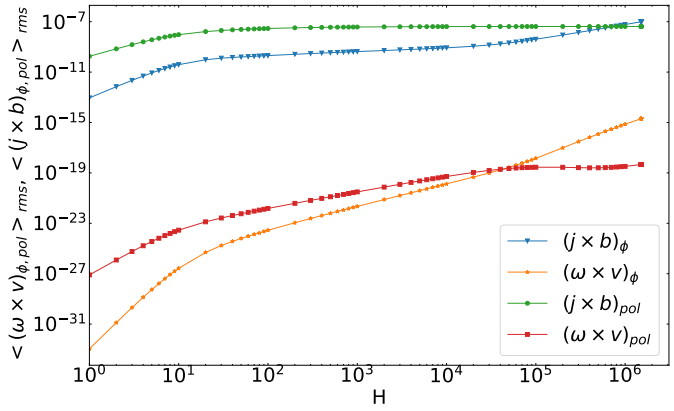

Figure 6: Root-mean square of toroidal and poloidal parts of $\boldsymbol{\omega}\times\mathbf{v}$ and $\mathbf{j}\times\mathbf{b}$ terms as a function of the Hartmann number in Alfvén velocity v_{A0} units with η=6.9e-9.

To verify if inertial effects could be involved in this regime shift at high Hartmann numbers, let us quantify the impact of the non-linear term on the overall velocity. In Fig. 5, we depict the contributions of the $(\boldsymbol{\omega}\times\mathbf{v})\cdot\mathbf{i}_\varphi$ and $(\mathbf{j}\times\mathbf{b})\cdot\mathbf{i}_\varphi$ terms to the total toroidal velocity in Eq.(36) for $H = 10^5$. Here, two assumptions are made: firstly, we set the $(\mathbf{j}\times\mathbf{b})\cdot\mathbf{i}_\varphi$ term to zero. Consequently, Eq.(37) is modified to

$$\hat{\nu}\hat{\triangle}^*\tilde{u}_4 = \frac{1}{x}\{\tilde{u}_1, \tilde{u}_4\} \tag{58}$$

Similarly, for the distribution on the right in Fig. 5, we make a similar assumption, but this time for the non-linear term

$$\hat{\nu}\hat{\triangle}^*\tilde{u}_4 = \frac{1}{x}\{\tilde{u}_3, \tilde{u}_5\} \tag{59}$$

It is worth noting that, even for high Hartmann numbers, the non-linear term is observed to be significantly smaller than the $(\mathbf{j}\times\mathbf{b})\cdot\mathbf{i}_\varphi$ term. The distribution on the right in Fig. 5 precisely corresponds to the toroidal velocity in Fig. 1, indicating that the non-linear term's contribution to the total velocity is negligible. Fig. 6 shows a comparison of the toroidal and poloidal parts of $\boldsymbol{\omega}\times\mathbf{v}$ and $\mathbf{j}\times\mathbf{b}$ terms as a function of the Hartmann number. Expressing these terms in new variables, the toroidal part of $\boldsymbol{\omega}\times\mathbf{v}$ becomes $\{u_1, u_4\}/x^2$, while the poloidal part is given by $u_2\nabla u_1/x^2 - u_4\nabla u_4/x^2$. Similarly, for $\mathbf{j}\times\mathbf{b}$, the toroidal component is $\{u_5, u_3\}/x^2$, and the poloidal one is $-u_3\nabla u_3/x^2 + u_6\nabla u_5/x^2$. It can be seen that the non-linear term grows with the increase of the Hartmann number, yet it remains sufficiently small not to impact the total toroidal and poloidal velocity. We conclude that the third regime is numerical.

4. Scaling laws

4.1. Prediction of the scaling laws with $H \ll 1$ and $H \gg 1$

Here, we would like to shift our focus to the first and second regimes and predict their scaling laws. The scaling of velocity in the first regime where $H \ll 1$ can be deduced analytically and is already documented in the literature [7]. According to [7], the toroidal velocity in this limit scales with H^4 while the poloidal velocity scales with H^2.

As depicted in Fig. 1, the second regime exhibits a distinct boundary layer that becomes thinner with the increase of the Hartmann number. To predict the velocity behaviour in this regime where $H \gg 1$ while the effects of inertial terms remain negligible, it is necessary to consider the boundary layer equations. Now, we aim to estimate the boundary layer thickness δ as a function of the Hartmann number, denoted as $\delta = \delta(H)$. We start from Eq. (54), at a given $\mathbf{E}/\eta$ and by neglecting the inertial term we have

$$-\left(\frac{\mathbf{E}}{\eta} + H\widetilde{\mathbf{v}}\times\mathbf{b}\right)\times\mathbf{b} = -\nabla p^* + H^{-1}\nabla^2\widetilde{\mathbf{v}}. \tag{60}$$

To facilitate the writing of equations within the boundary layer, we introduce a new coordinate system in which the plasma boundary $\partial\Omega$ aligns with the y-axis while x denotes the transverse direction. We introduce the characteristic length, L, in the y-direction and the boundary layer thickness δ in the x-direction ($\delta \ll L$) (see Fig. 7).

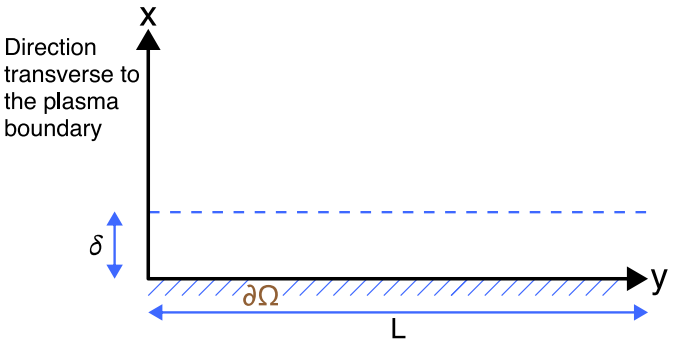

Figure 7: Sketch of the slab geometry used in the boundary layer equations.

V_c and B_c represent the characteristic plasma speed and magnetic field along y. Let $\widetilde{v}_x$ and $\widetilde{v}_y$ denote the velocity components in the x and y directions respectively, and b_x and b_y the magnetic field components. From Eq. (60) we derive

$$-H\left(\widetilde{v}_y b_y b_x - b_y b_y \widetilde{v}_x\right) = -\frac{\partial p^*}{\partial x} + H^{-1}\left(\frac{\partial^2 \widetilde{v}_x}{\partial x^2} + \frac{\partial^2 \widetilde{v}_x}{\partial y^2}\right), \quad (61)$$

$$-H\left(\widetilde{v}_x b_x b_y - b_x b_x \widetilde{v}_y\right) = -\frac{\partial p^*}{\partial y} + H^{-1}\left(\frac{\partial^2 \widetilde{v}_y}{\partial x^2} + \frac{\partial^2 \widetilde{v}_y}{\partial y^2}\right), \quad (62)$$

where, in Eq. (62), we can anticipate that the pressure gradient along y is negligible. By assuming $\widetilde{v}_y \sim V_c$, $y \sim L$, $x \sim \delta$, $b_y \sim B_c$, we estimate $\widetilde{v}_x$ from the incompressibility condition

$$\frac{\partial \widetilde{v}_x}{\partial x} + \frac{\partial \widetilde{v}_y}{\partial y} = 0 \quad (63)$$

and similarly b_x from the zero-divergence of the magnetic field

$$\frac{\partial b_x}{\partial x} + \frac{\partial b_y}{\partial y} = 0 \quad (64)$$

as $\widetilde{v}_x \sim \delta V_c/L$ and $b_x \sim \delta B_c/L$. Now the Equation (62) yields

$$HV_c\frac{\delta^2}{L^2}B_c^2 \sim H^{-1}\frac{V_c}{\delta^2} + H^{-1}\frac{V_c}{L^2}. \quad (65)$$

The largest viscous term should be comparable in the magnitude to the left hand term, that is

$$HV_c\frac{\delta^2}{L^2}B_c^2 \sim H^{-1}\frac{V_c}{\delta^2} \quad (66)$$

which gives the boundary layer thickness scaling as

$$\delta \sim \frac{1}{\sqrt{H}}. \quad (67)$$

Let us note that this is in agreement with the numerical estimate of the boundary layer thickness obtained in [15] as a function of the viscosity as $\delta \sim \nu^{1/4}$ (assuming there η constant). Let us now estimate the behaviour of the velocity root-mean-square with H. Let us focus on the velocity $\widetilde{v}$ in the poloidal direction. By definition, its root-mean-square is

$$< \widetilde{v}_{pol} >_{rms} = \left(\frac{\int_\Omega \widetilde{v}_{pol}^2 ds}{\int_\Omega ds}\right)^{1/2}. \quad (68)$$

In the boundary layer (BL), using the expression of the poloidal velocity in terms of the stream function (26) yields $\widetilde{v}_{pol}^{BL} \sim H/(\eta\delta)$ while in the rest of the plasma the contribution of the transverse gradient should be of order 1 yielding $\widetilde{v}_{pol}^{core} \sim H/(\eta\delta)$. This yields

$$\int_\Omega \widetilde{v}_{pol}^2 ds = \int_{BL} \widetilde{v}_{pol}^2 ds + \int_{\Omega core} \widetilde{v}_{pol}^2 ds \sim \frac{L\delta H^2}{\eta^2\delta^2} + \frac{L^2H^2}{\eta^2} \sim \frac{LH^2}{\eta^2\delta}. \quad (69)$$

Consequently, $< \widetilde{v}_{pol} >_{rms} \sim H/\eta\delta^{-1/2}$, so that in the original velocity variable and using (67), one obtains the scaling

$$< v_{pol} >_{rms} \sim \eta H^{1/4}. \quad (70)$$

The root-mean-square of the toroidal velocity should follow the same scaling as the poloidal velocity because poloidal and toroidal components are interchangeable from the perspective of the boundary layer analysis and can both align with the y-axis of Fig. 7. By this argument, we can conclude that $< v_{pol} >_{rms}$ and $< v_\phi >_{rms}$ scales with $\eta H^{1/4}$ for $H \gg 1$. Let us finally note that we have made use of the incompressibility assumption in Eq. (63) to derive this scaling law so that we do not expect these results to be transferable to the case of compressible flow.

4.2. Numerical estimation of the scaling laws

Let us estimate the scaling laws of the velocity in these two regimes by using a power-law fitting. In Fig. 8 it can be seen that in the limit as the Hartmann number H approaches zero for the first regime, the velocity follows the pattern $\eta f(H)$, with f approximately equal to H^4 for toroidal velocity and H^2 for poloidal velocity. In the second regime, the velocities scale as $H^{1/4}$. It corresponds to the analytical predictions made in Section 4.1.

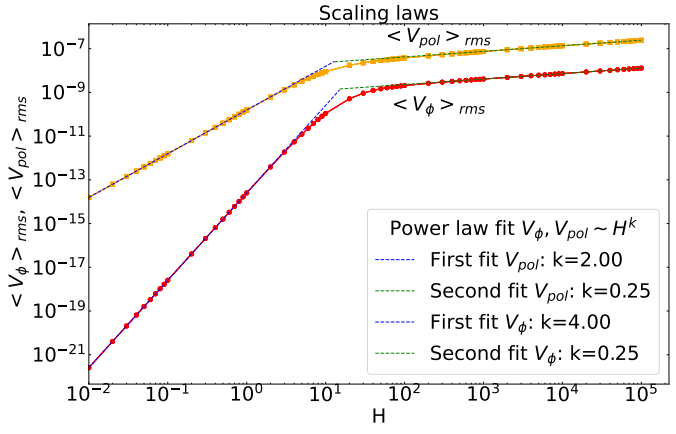

Figure 8: Root-mean square of toroidal and poloidal velocities in Alfvén velocity units as a function of the Hartmann number in log-log scale with power-law fitting curves.

4.3. *Effect of boundary conditions*

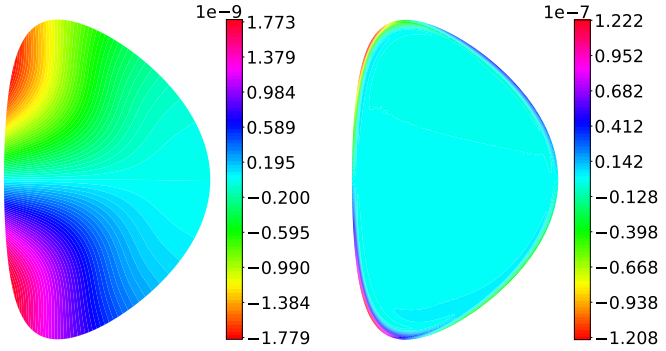

Figure 9: Toroidal velocity field computed with the finite element method (FEM) using FreeFem++ with P1 elements for $H = 10$ (on the left) and $H = 10^4$ (on the right) in JET geometry with free-slip boundary condition for toroidal velocity with η=6.9e-9 and E_0=3e-9.

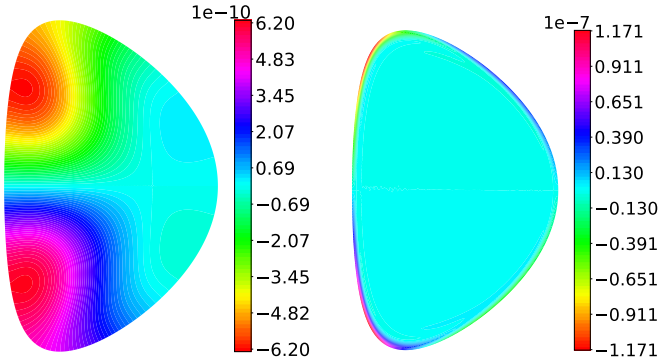

Figure 10: Toroidal velocity field computed with the finite element method (FEM) using FreeFem++ with P1 elements for $H = 10$ (on the left) and $H = 10^4$ (on the right) in JET geometry with $\partial_n(u_4/x) = 0, u_2 = 0$ boundary conditions with η=6.9e-9 and E_0=3e-9.

Let us take a closer look at the behaviour of the toroidal velocity field with different boundary conditions: Fig. 9 presents the same as Fig. 1 for $H = 10$ and $H = 10^4$ but with the "free-slip" boundary conditions for the toroidal velocity ($\partial_n(u_4/r^2) = 0, u_2 = 0$). Fig. 10 presents the application of $\partial_n(u_4/x) = 0, u_2 = 0$ boundary conditions and finally Fig. 11 illustrates the zero normal derivative of the toroidal velocity and vorticity ($\partial_n(u_4/x) = \partial_n(u_2/x) = 0$) boundary conditions.

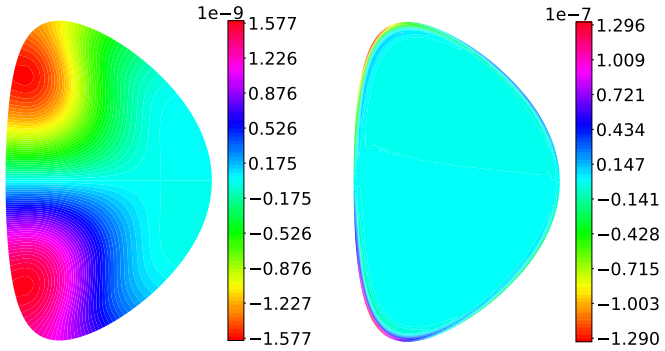

Figure 11: Toroidal velocity field computed with the finite element method (FEM) using FreeFem++ with P1 elements for $H = 10$ (on the left) and $H = 10^4$ (on the right) in JET geometry with $\partial_n(u_4/x) = \partial_n(u_2/x) = 0$ boundary conditions with η=6.9e-9 and E_0=3e-9.

In Fig. 12, we present a comparison of the diverse boundary conditions described above in Section 3.1, applied to the toroidal velocity and vorticity. To facilitate interpretation, we have normalized the root-mean-square of the toroidal velocity field with respect to the corresponding resistivity values. Notably, this normalization leads to the convergence of the curves across the resistivity values.

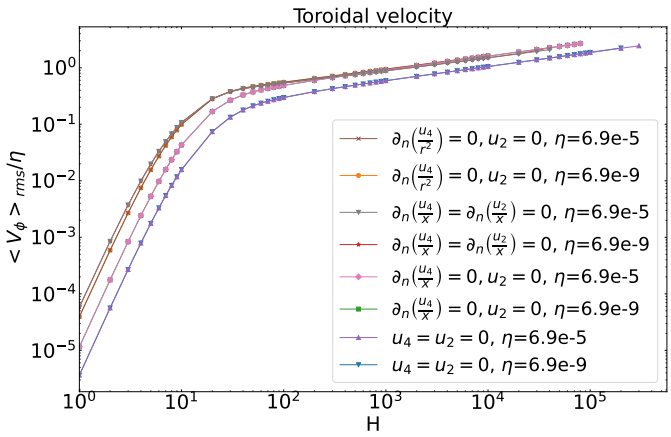

Figure 12: Root-mean square of the toroidal velocity field (in Alfvén velocity units) over η as a function of the Hartmann number in log-log scale for different boundary conditions for the toroidal velocity and vorticity, for different values of the resistivity and a given $E_0/\eta = 0.43$.

It can be seen that the scaling law for the toroidal velocity slightly varies with the application of different boundary conditions, yet this variation is small enough to state that the scaling maintains the same order. The characteristics of the first and second slopes now reveal that, at a fixed E_0/η ratio, the velocity is dependent on the Hartmann number only, and this scaling remains even when taking into account different boundary conditions.

4.4. *Effect of the control parameter*

In the present study, we have been interested in the behaviour of the system for a given ratio of E_0/η. This quantity may be viewed as the only explicit drive appearing in the dimensionless system of equations (44)-(49), being the dominant term of

$u_6 = x j_\varphi$, that is the toroidal current source term of the Grad-Shafranov equation (49). The behaviour $v/\eta \propto H^4$ in the limit of small H was numerically derived in Section 4 for E_0/η of order 1. If E_0/η is allowed to vary, then we have a problem with two parameters, H and E_0/η. Let us now consider different values of E_0/η. Fig. 13 shows the root-mean square of the toroidal velocity field divided by η, divided by $(E_0/\eta)^3$. This particular normalization happens to make all the curves collapse in the $H \to 0$ limit.

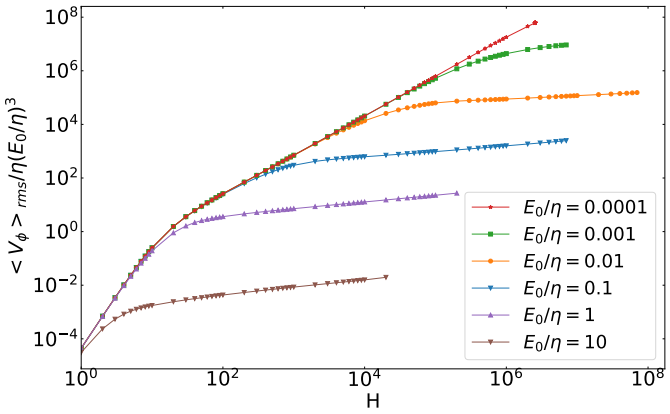

Figure 13: Root-mean-square of toroidal velocity field normalized on $\eta(E_0/\eta)^3$ as a function of the Hartmann number in Alfvén velocity v_{A0} units for the different values of the ratio E_0/η.

When E_0/η is small but H is no longer small, we observe the emergence of a new scaling law in H, coming between the previous small H scaling (that we called the first regime) and the large H boundary-layer governed scaling (that we called the second regime). This new intermediary regime is all the more extensive as E_0/η is small and does not involve a boundary layer. These results emphasize the critical role of the E_0/η ratio in influencing the toroidal velocity regimes, scaling and boundary layer formation. That being said, the relevant order of magnitude for E_0/η in tokamaks is about one.

5. Conclusion and perspectives

Within the framework of a visco-resistive magnetohydrodynamic model applied to a tokamak plasma with a prescribed toroidal current drive, we have successfully predicted and numerically validated a scaling law for the velocity. This scaling law is expressed as a function of the resistivity, η, and the Hartmann number, H, where H is defined as $H \equiv (\eta\nu)^{-1/2}$, with ν denoting viscosity. The observed behaviour indicates that the velocity scales as $\eta f(H)$, where f is a specific function. Notably, this scaling law remains valid under the condition that the inertial term $\omega \times \mathbf{v}$ remains negligible which happens to be the case up to the largest numerically accessible values of the Hartmann number. Within this general scaling law, we have numerically uncovered, for a given, order-one, E_0/η drive, two limiting regimes at low and high H where the function f behaves as a power law.

Overall, the order of magnitude of the plasma velocity remains low compared to experimental measurements and to the expected velocities necessary for taming instabilities. It is obviously possible to attribute this to the absence of turbulence in this axisymmetric -and thus 2D- model, to the lack of symmetry breaking, or to the use of a MHD, rather than kinetic, modeling. An additional explanation may lie in some insufficiency in the description of the plasma heating drive. This will be the subject of a forthcoming study. Let us finally emphasize that we are here deliberately exploring scenarios of plasma rotation within the axisymmetric framework, since this could 'nip in the bud' 3D instabilities.

Acknowledgments

This work has been carried out within the framework of the EUROfusion Consortium and has received funding from the Euratom research and training programme 2014-2018 under grant agreement No 633053. The views and opinions expressed herein do not necessarily reflect those of the European Commission.

References

[1] A. Bondeson, D. J. Ward, Stabilization of external modes in tokamaks by resistive walls and plasma rotation, Phys. Rev. Lett. 72 (1994) 2709–2712. doi:10.1103/PhysRevLett.72.2709.
URL https://link.aps.org/doi/10.1103/PhysRevLett.72.2709

[2] S. A. Sabbagh, R. E. Bell, J. E. Menard, D. A. Gates, A. C. Sontag, J. M. Bialek, B. P. LeBlanc, F. M. Levinton, K. Tritz, H. Yuh, Active stabilization of the resistive-wall mode in high-beta, low-rotation plasmas, Phys. Rev. Lett. 97 (2006) 045004. doi:10.1103/PhysRevLett.97.045004.
URL https://link.aps.org/doi/10.1103/PhysRevLett.97.045004

[3] M. Takechi, G. Matsunaga, N. Aiba, T. Fujita, T. Ozeki, Y. Koide, Y. Sakamoto, G. Kurita, A. Isayama, Y. Kamada, Identification of a low plasma-rotation threshold for stabilization of the resistive-wall mode, Phys. Rev. Lett. 98 (2007) 055002. doi:10.1103/PhysRevLett.98.055002.
URL https://link.aps.org/doi/10.1103/PhysRevLett.98.055002

[4] J. Rice, A. Ince-Cushman, J. deGrassie, L.-G. Eriksson, Y. Sakamoto, A. Scarabosio, A. Bortolon, K. Burrell, B. Duval, C. Fenzi-Bonizec, M. Greenwald, R. Groebner, G. Hoang, Y. Koide, E. Marmar, A. Pochelon, Y. Podpaly, Inter-machine comparison of intrinsic toroidal rotation in tokamaks, Nuclear Fusion 47 (11) (2007) 1618. doi:10.1088/0029-5515/47/11/025.
URL https://dx.doi.org/10.1088/0029-5515/47/11/025

[5] C. Angioni, R. M. McDermott, F. J. Casson, E. Fable, A. Bottino, R. Dux, R. Fischer, Y. Podoba, T. Pütterich, F. Ryter, E. Viezzer, Intrinsic toroidal rotation, density peaking, and turbulence regimes in the core of tokamak plasmas, Phys. Rev. Lett. 107 (2011) 215003. doi:10.1103/PhysRevLett.107.215003.
URL https://link.aps.org/doi/10.1103/PhysRevLett.107.215003

[6] L. P. Kamp, D. C. Montgomery, Toroidal flows in resistive magnetohydrodynamic steady states, Physics of Plasmas 10 (2003) 157–167.

[7] L. P. Kamp, D. C. Montgomery, J. W. Bates, Toroidal flows in resistive magnetohydrodynamic steady states, Physics of Fluids 10 (7) (1998) 1757–1766. arXiv:https://pubs.aip.org/aip/pof/article-pdf/10/7/1757/12487686/1757_1_online.pdf, doi:10.1063/1.869692.
URL https://doi.org/10.1063/1.869692

[8] J. A. Morales, W. J. T. Bos, K. Schneider, D. C. Montgomery, Intrinsic rotation of toroidally confined magnetohydrodynamics, Phys. Rev. Lett. 109 (2012) 175002. doi:10.1103/PhysRevLett.109.175002.
URL https://link.aps.org/doi/10.1103/PhysRevLett.109.175002

[9] M. Holst, V. Kungurtsev, S. Mukherjee, A Note on Optimal Tokamak Control for Fusion Power Simulation, arXiv e-prints (2022) arXiv:2211.08984arXiv:2211.08984, doi:10.48550/arXiv.2211.08984.

[10] H. Oueslati, T. Bonnet, N. Minesi, M.-C. Firpo, A. Salhi, Numerical derivation of steady flows in visco-resistive magnetohydrodynamics for JET and ITER-like geometries with no symmetry breaking, AIP Conf. Proceedings 2179 (2019) 020009.

[11] H. Oueslati, M.-C. Firpo, Breaking up-down symmetry with magnetic perturbations in tokamak plasmas: Increase of axisymmetric steady-state velocities, Physics of Plasmas 27 (2020) 102501.

[12] E. Roverc'h, H. Oueslati, M.-C. Firpo, Steady-state flows in a visco-resistive magnetohydrodynamic model of tokamak plasmas with inhomogeneous heating, J. Plasma Physics 87 (2021) 905870217.

[13] F. Hecht, New development in Freefem++, J. Numer. Math. 20 (3-4) (2012) 251–265.

[14] S. Cappello, D. F. Escande, Bifurcation in viscoresistive MHD: The Hartmann number and the Reversed Field Pinch, Phys. Rev. Lett. 85 (2000) 3838–3841. doi:10.1103/PhysRevLett.85.3838.
URL https://link.aps.org/doi/10.1103/PhysRevLett.85.3838

[15] L. P. J. Kamp, D. Montgomery, Toroidal steady states in visco-resistive magnetohydrodynamics, Journal of Plasma Physics 70 (2) (2004) 113–142. doi:10.1017/S0022377803002629.